

A New Type of Weyl Semimetals

Alexey A. Soluyanov¹, Dominik Gresch¹, Zhijun Wang³, QuanSheng Wu¹, Matthias Troyer¹, Xi Dai², and B. Andrei Bernevig³

¹*Institute for Theoretical Physics, ETH Zürich, 8093 Zürich, Switzerland*

²*Institute of Physics, Chinese Academy of Sciences, Beijing 100190, China and*

³*Department of Physics, Princeton University, New Jersey 08544, USA*

(Dated: May 24, 2022)

The Dirac equation of quantum field theory gives rise to massless Weyl fermions that respect Lorentz invariance. In condensed matter these fermions are realized as low energy excitations in Weyl semimetals. In these materials a topologically protected linear crossing of two bands, called a Weyl point, occurs at the Fermi level resulting in a point-like Fermi surface. Lorentz invariance, however, can be violated in condensed matter, and here we generalize the Dirac equation accordingly to obtain a fundamentally new kind of Weyl fermions. In particular, we report on a novel type of Weyl semimetal, with a new type of Weyl point that emerges at the boundary between electron and hole pockets. This node, although still a protected crossing, has an open, not point-like, Fermi surface, suggesting physical properties very different from that of standard Weyl points. We show that an established material, WTe₂, is an example of this novel type of topological semimetals.

The recent intense search for topological states of matter has mostly focused on theoretically predicting and experimentally discovering new classes of topological insulators. However, topologically interesting behavior occurs not only in insulators – metallic band structures also exhibit non-trivial topological features [1]. Of these metals, the ones with vanishingly small density of states at the Fermi level, called semimetals (SM), stand out. For these materials, a distinction between topologically protected surface and bulk metallic states can still be made, and their Fermi surfaces (FS) allow for a topological characterization.

Two kinds of TSM with the simplest possible FS have attracted special attention: Dirac [2–8] and Weyl SMs [9–20]. In these materials a linear crossing of two (Weyl) or four (Dirac) bands occurs at the Fermi level, as shown in the left panel of Fig. 1. The corresponding effective Hamiltonian for these crossings is given by the Weyl or Dirac equation respectively. In the following we limit the discussion to Weyl crossings only, although our results hold for Dirac crossings as well.

The appearance of Weyl points (WPs) is only possible in a material if the product of parity and time-reversal (TR) is not a symmetry of the structure. When present, a WP acts as a topological charge, being either a source or a sink of Berry curvature. Thus, a FS enclosing a WP has a well-defined Chern number, corresponding to this point's topological charge. Since the net charge has to vanish in the entire Brillouin zone (BZ), WPs always come in pairs; WPs are stable to weak perturbations and can only be annihilated in pairs of opposite charge. A large number of unusual physical phenomena are associated with Weyl TSM, including the existence of open Fermi arcs in the surface FS [9, 21, 22], and different anomalies in magnetotransport [23–30].

Weyl SMs with broken TR symmetry have been predicted to exist in several materials [9–12], but experimental verification has so far been lacking. Scenarios of realizing this phase without breaking TR [31] that re-

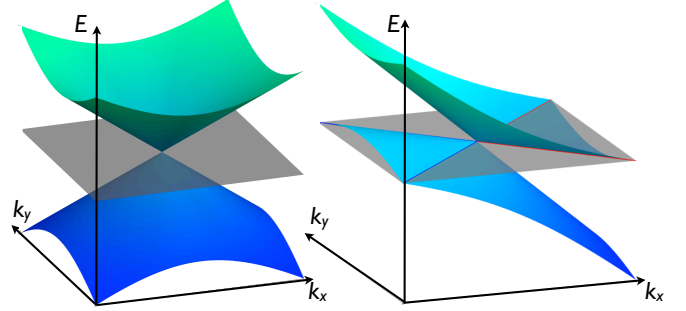


Figure 1. Possible types of Weyl semimetals. Left panel: Type I Weyl point with point-like Fermi surface. Right panel: Type II Weyl point is the touching point between electron and hole pockets.

quired either alloying or application of external pressure were also proposed [13–15]. More recently, the Weyl SM was predicted to exist in single crystal nonmagnetic materials of the TaAs class [16, 17], and this prediction was soon verified experimentally [18, 19].

Up to now, Weyl SMs have been thought to have a point-like FS at the WP. We refer to these as type-I WPs (WP1), to contrast them with the new type-II WPs (WP2) that exist at the boundary of electron and hole pockets, as illustrated in the right panel of Fig. 1. We discuss general conditions for WP2s to appear, and present evidence that WTe₂ is an example of the the new type of TSM hosting eight WP2s. They come in two quartets located 0.052 eV and 0.058 eV above the Fermi level. Topological arguments will be given to prove the existence of the novel TSM phase in this material. The possibility of doping-driven topological Lifshits transitions, characteristic of WP2s, as well as emerging Fermi arcs at the surface, are illustrated in detail. Interestingly, WTe₂ was recently reported [32] to have the largest known to date, never-saturating magnetoresistance.

We start by considering the most general Hamiltonian describing a WP

$$H(\mathbf{k}) = \sum_{ij} \mathbf{k}_i \mathbf{A}_{ij} \sigma_j \quad (1)$$

where A_{ij} is a 3×4 matrix, with $i = x, y, z$, and $j = 0, x, y, z$ being indices of the 2×2 unit and three Pauli matrices. The spectrum is given by

$$\varepsilon_{\pm}(\mathbf{k}) = \sum_{i=1}^3 k_i A_{i0} \pm \sqrt{\sum_{j=1}^3 \left(\sum_{i=1}^3 k_i A_{ij} \right)^2} = T(\mathbf{k}) \pm U(\mathbf{k}) \quad (2)$$

The kinetic part of energy, $T(\mathbf{k})$, tilts the cone-like spectrum. Breaking the Lorentz invariance of the Dirac equation that gives rise to Weyl fermions in quantum field theory, this tilt has previously been ignored. Since Lorentz invariance does not need to be respected in condensed matter, its inclusion is important and leads to a finer classification of distinct FSs in a one-to-one correspondence with the theory of quadric surfaces [33]. For a direction in reciprocal space, where T is dominant over U , the tilt becomes large enough to produce touching electron and hole pockets, rather than a point-like FS. Thus, the condition for a WP to be of type II is that there exists a direction $\hat{\mathbf{k}}$, for which $T(\hat{\mathbf{k}}) > U(\hat{\mathbf{k}})$. If such a direction does not exist, the WP is of Type I. The clear *qualitative* distinction in FSs of the two types of WPs suggests very different responses to magnetic fields [34].

We now proceed to describe WTe_2 , a material that we identified to host WPs of this new type. The crystal structure of WTe_2 is orthorhombic and belongs to the space group $Pnm2_1 (C_{2v}^7)$. Its primitive unit cell contains four formula units. The atomic structure can be viewed as layered, with single layers of W separated from each other by Te bilayers and stacked along the z -axis (see Appendix A). The distance between adjacent W atoms is considerably smaller along the x -axis than along the others, creating strong anisotropy. The unit cell has two reflection symmetries: mirror in the yz -plane, and a glide plane formed by a reflection in the xz -plane followed by a translation by $(0.5, 0, 0.5)$ (in reduced coordinates). Combined they form a non-symmorphic two-fold rotation C_2 , which is important in the following symmetry arguments.

The result of band structure calculations (see Appendix B for details) without spin-orbit coupling (SOC) is shown in Fig. 2(a) along the Γ - X direction, where an intermediate point $\Sigma = (0.375, 0, 0)$ is introduced. Apart from electron-hole pockets, 16 WPs are found in WTe_2 in the absence of SOC not accounting for spin (not shown in Fig. 2(a)). Half of these points occur at points of low symmetry at $k_z \neq 0$. The other half of SOC-free Weyls appear in the $k_z = 0$ plane, where the product of TR and C_2 ($C_{2T} = C_2 * T$) forms a little group. While generically degeneracies on high symmetry planes are forbidden, it can be shown that due to the C_{2T} symmetry two-fold degeneracies are locally stable at points in the $k_z = 0$

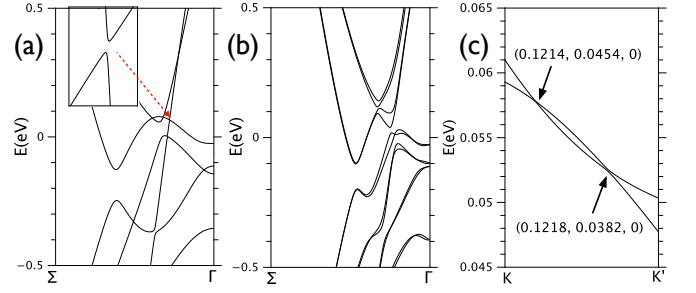


Figure 2. Panel (a): Band structure of WTe_2 without SOC. A fraction of Γ - X segment is shown: the point Σ has coordinates $(0.375, 0, 0)$. Band gap of $\approx 1\text{meV}$ is shown in the inset signaling a gapless point nearby. Panel (b): Band structure of WTe_2 with SOC. Panel (c): One of the four pairs of WPs. Their locations are designated in reduced coordinates. Zero energy is set to E_F in all panels.

plane [33]. On the Γ - X line the spectrum is generally gapped with a band gap of $\approx 1\text{meV}$, separating valence and conduction bands as shown in Fig. 2(a).

If spin is taken into account, but no SOC is included, all bands become doubly degenerate corresponding to opposite spin projections. This doubles the topological charge of each Weyl, since by $\text{SU}(2)$ symmetry WPs corresponding to opposite spins have the same topological charge. Introduction of infinitesimal SOC cannot gap them, hence giving a general recipe to search for Weyl semimetals [33].

In WTe_2 , however, SOC is not small. When turned on, it preserves electron-hole pockets, but significantly changes the structure of WPs. At intermediate SOC WPs can move, emerge or annihilate in pairs of opposite chirality. As a result, at full SOC all WPs at $k_z \neq 0$ are annihilated. In the $k_z = 0$ plane, double degeneracies at isolated k -points are still allowed by symmetry [33]. Eight such gapless points are found, formed by the top-most valence and lowest conduction bands at full SOC. A pair of such points is shown in Fig. 2(c). The other three pairs are related to this one by reflections. Energetically both points are located only slightly (0.052 and 0.058 eV) above the Fermi energy. A more detailed description of the band structure and WPs can be found in the Appendix C.

To rigorously establish the degeneracies of WPs and the non-trivial topology of the band structure, we examine the structure of the Berry curvature $\mathcal{F}(\mathbf{k})$ of Bloch states around the gapless points. Since a WP represents a monopole in Berry curvature, the flux of \mathcal{F} through a surface enclosing it in k -space has to be quantized and equal to the total topological charge enclosed. For this reason the FS of WP1, being a closed surface, has non-zero Chern number. In case of WP2, however, the FS is open, and hence cannot be used to compute the topological charge of a WP. Instead, we integrate the Berry curvature of N bands, where N is the number of electrons per unit cell. A surface, on which these N bands

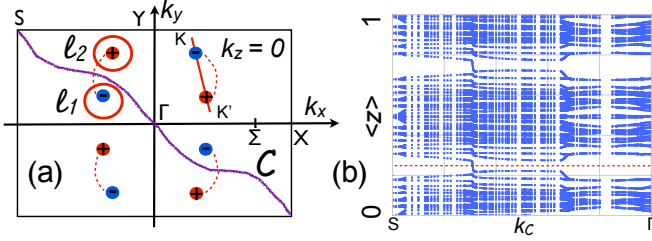


Figure 3. Panel (a): schematic illustration of the BZ cross-section at $k_z = 0$ and Weyl points in it, their chirality marked with red and blue color, corresponding to $C = +1$ and $C = -1$. The red line corresponds to the BZ segment shown in Fig. 2(c). Panel (b): Wannier charge centers (Wilson loop) on the plane, shown schematically as contour C in panel (a). It corresponds to a non-trivial \mathbb{Z}_2 invariant.

are separated by an energy gap from the higher energy bands and which encloses the WP2 can always be found and can be used to compute the topological charge of a WP2 (see Appendix D).

For WTe₂ these surfaces were taken to be spheres enclosing the Weyl points, as shown by contours ℓ_1 and ℓ_2 in Fig. 3(a). For the sphere ℓ_1 the Chern number is found to be $C = -1$, thus proving the existence of a WP of negative chirality inside it. A similar calculation for the sphere ℓ_2 , enclosing the second WP, results in a positive topological charge $C = +1$. This calculation combined with the use of symmetries allowed us to map out the structure of the eight WPs in the BZ of WTe₂. They are drawn schematically in Fig. 3(a).

To understand which pairs of opposite chirality Weyl nodes are connected by the Berry flux, thus defining the structure of the surface Fermi arcs, several topological invariants are computed directly from first-principles calculations. The presence of TR allows for the computation of the \mathbb{Z}_2 -invariant [35] on TR-symmetric planes in the BZ, defined by the condition $k_i = 0, \pi$, where $i = x, y, z$. One such plane, the $k_z = 0$ one, hosts gapless points, and the invariant is not well defined for it. For the other five planes, where the $N = 72$ bands are gapped from the band $N + 1$, the topological invariant is computed using a hybrid Wannier centers technique [36] and found to be trivial. The corresponding Wilson loops [37] are gapped.

A non-trivial topological invariant can, however, be defined for WTe₂. It is also a TR \mathbb{Z}_2 invariant, which describes the motion of Wannier charge centers on a curved surface that goes in between neighboring WPs, as shown schematically by contour C in Fig. 3(a). This surface consists of strings in the k_z -direction, and its projection onto the (k_x, k_y) -plane forms a smooth TR-symmetric curve, meaning that if the curve passes through a point (k_x, k_y) then it passes through its TR-image $(-k_x, -k_y)$ as well. The surface thus satisfies the conditions of the \mathbb{Z}_2 -pump defined in Ref. [38].

The calculation of this invariant was carried out directly from first-principles calculations using the Z2Pack

software package [39]. The results in Fig. 3(d) show that pumping in this plane occurs between two TR invariant momenta: $k_x = k_y = -\pi$ (S) and $k_x = k_y = 0$ (Γ). Thus, the plane (C, k_z) exhibits a quantum spin Hall effect. If an open surface in the z -direction is introduced, helical surface states appear along the curve C in the surface BZ, becoming part of the Fermi arcs. Given that the $k_{x,y} = 0$ planes have gapped Wilson loops, we conclude that the Berry flux connects pairs of neighboring WPs, as illustrated schematically in Fig. 3(a). This calculation gives another, first-principles based, proof that WPs exist in WTe₂, resolving their connectivity and the location of Fermi arcs.

To see that these WPs are of type II, the dispersion around these points was obtained from first-principles calculations and compared to the analytic expression. The latter can be derived using the symmetry analysis presented in the Appendix C. Taking k_i to be the coordinate relative to the position of the WP and only keeping terms linear in k we get

$$\varepsilon_{\mathbf{k}} = Ak_x + Bk_y \pm \sqrt{e^2k_z^2 + (ak_x + ck_y)^2 + (bk_x + dk_y)^2} \quad (3)$$

Comparison with the *ab initio* results allows us to find the values for parameters A, B, a, b, c, d and e given in the Appendix C. The kinetic part of the energy dominates, most prominently along the line connecting the nearest WP. This agrees with the spectrum illustrated in Fig. 2(c). We thus conclude that WTe₂ is a type II Weyl SM.

Having established the existence of this novel TSM phase and the charges associated with each of the WP2 in WTe₂, we proceed to discuss the FS topology and possible topological Lifshits transitions in this compound. The evolution of the FS obtained from first-principles calculations is shown in Fig. 4 for different values of E_F . Since the WPs are located in the $k_z = 0$ plane and due to reflection symmetries, only a part of the $k_z = 0$ cut of the FS is shown. For $E_F = 0$ eV the FS is formed by two pairs of electron and two pairs of hole pockets (that is, 8 pockets overall), separated in momentum space, and for each pair a larger surface completely encloses the smaller one. This is illustrated in Fig. 4(a), where 4 halved (2 n - and 2 p -) pockets are shown. The other halves are related to the ones shown by the glide plane g_{xz} , while the other 4 pockets appear at positive k_x related to the ones shown by the mirror symmetry m_{yz} . All Fermi surfaces have zero Chern numbers in this case.

When E_F is raised, two additional electron pockets appear, while the previously existing electron pockets persist. The hole pockets shrink quickly, two out of the four of them disappearing completely. Each of the other two split into two disconnected pockets. As a result, there are 6 electron- and 4 hole-pockets in total (see Fig. 4(b) for illustration). For the Fermi level tuned to the energy of the first WP $E_F = 0.052$ eV, which corresponds to the addition of ≈ 0.064 electrons per unit cell, each of the two newly appeared n -pockets touches two p -pockets at

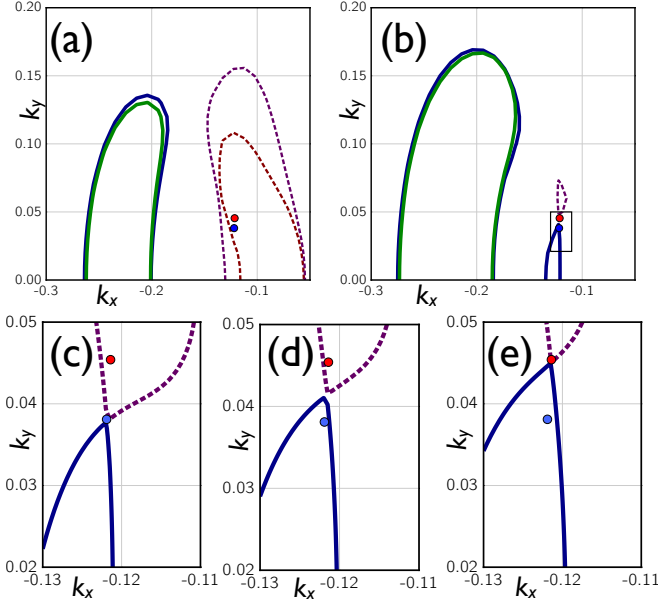


Figure 4. Fermi surface at $k_z = 0$. A part of the BZ is shown. (a). $E_F = 0\text{eV}$: electron (blue and green solid) and hole (red and magenta dashed) pockets come in pairs. (b). The structure of electron and hole pockets at higher energies ($E_F = 0.055\text{eV}$ shown). There are four hole (1 shown) and 6 electron (halves of the 3 of them shown) pockets. The zoom of the framed region is shown in (c)-(e) for different values of E_F . (c). $E_F = 0.052\text{eV}$ is set to the lower energy Weyl point. A touching between n - and p - pockets occurs at the Weyl point. (d). $E_F = 0.055\text{eV}$ is set to be in between the two Weyl points. The n - and p -pockets are disconnected. The hole pocket encloses a $C = +1$ Weyl point. The electron pocket encloses the $C = -1$ point and its mirror image (not shown), so the net Chern number of this pocket is zero. (e). At the higher energy Weyl point $E_F = 0.058\text{eV}$ electron and hole pockets touch again (shown) to reopen at larger E_F having zero Chern numbers.

the positions of the WPs, as illustrated in Fig. 4(c) for the part of $k_z = 0$ plane. Further increase of E_F disconnects the electron and hole pockets again, as shown in Fig. 4(d) for $E_F = 0.055\text{eV}$. The topology of the Fermi surfaces changes though: electron pockets still have zero Chern numbers, since they enclose two WPs of opposite charge, related by g_{xz} . The hole pockets have Chern numbers ± 1 . The Chern number of the p -pocket shown in Fig. 4(d) is $+1$. Topologies of the other p -pockets can be guessed from mirror and glide symmetries, keeping in mind that both these operations flip the sign of the Chern number. The pockets touch again (see Fig. 4(e)) when the Fermi level is tuned to the higher energy WP ($E_F = 0.058\text{eV}$, that is with ≈ 0.079 additional electrons per unit cell). When E_F is raised above this point, the pockets disconnect again, and all FS Chern numbers become zero.

Since WPs of opposite chirality are located very close to each other, WTe_2 is close to a topological transition

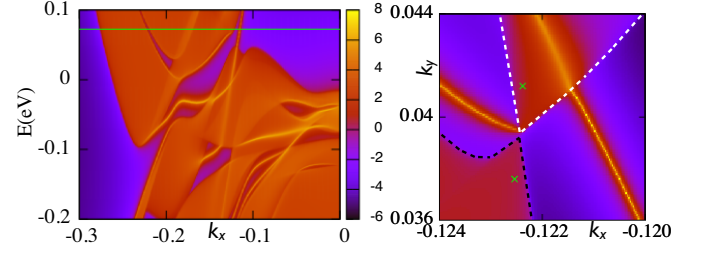


Figure 5. Left panel: spectral function of the (001) surface. Fermi level is set in between the Weyl points (shown in green). Right panel: (001) surface Fermi surface and a Fermi arc connecting p - and n -pockets. Green crosses mark the positions of Weyl points.

which occurs when points of opposite chirality annihilate each other. To facilitate the observation of topological Lifshitz transitions, hydrostatic pressure can be applied. Neighboring WPs are pushed away from each other in k -space under compression. In particular, a 0.5% (2%) compression moves the gapless points further away from each other, increasing the distance between them from 0.7% to 2% (4%) of the reciprocal lattice vector $|G_2|$, which is a large separation.

Finally, we discuss the topological surface states of WTe_2 . Due to the presence of reflection symmetries, WPs of opposite chirality are projected on top of each other on the (100) and (010) surfaces. This means that a cylinder of arbitrary radius in k -space with an axis along k_x or k_y , always encloses mutually canceling topological charges. Thus, no topologically protected surface states exist on these surfaces.

For the (001) surface all the WPs project onto distinct points, so topological Fermi arcs should appear. From the above FS analysis, we know that when E_F is tuned in between the WPs, one of the FS has non-zero Chern number. Hence, a surface state should emerge from it, connecting it either to one of its mirror images or to the WP of opposite Chern number located inside the n -pocket. Fig. 5 illustrates the (001) surface spectral function. Topological surface states connecting electron and hole bands are clearly visible in the surface spectrum in the left panel of Fig. 5. Setting E_F in between the WPs, one can clearly see a Fermi arc connecting the topological p -pocket to the n -pocket, as shown in the right panel of Fig. 5. Note that these are the same bulk pockets that are seen in Fig. 4(c-e). For fixed E_F this state can change its shape but cannot be removed. The other surface state crossing the p -pocket emerges from the n -pocket (not seen in the figure) and goes back into it, and thus can be pushed into the continuum of bulk states not to be seen at this E_F (see Appendix F). As noted previously, the application of external pressure moves the WPs apart, and can thus make the topological Fermi arc longer, facilitating its observation.

Of other transition metal dichalcogenides, that are generally semiconducting, only a high-temperature structure

of MoTe_2 [40, 41] was reported to be a semimetal resembling pressurized WTe_2 , which makes it another strong candidate material. However, we expect that many other material classes with electron-hole pockets host type II WPs, and can be used to explore new physical phenomena arising in this novel TSM phase.

Acknowledgements. AAS, DG, QSW and MT acknowledge the support of Microsoft Research, the Swiss National Science Foundation through the National Competence Center in Research MARVEL, the Euro-

pean Research Council through ERC Advanced Grant SIMCOFE. ZJW and BAB acknowledge the support of MURI-130-6082, ONR-N00014-11-1-0635, NSF CAREER DMR-0952428, NSF- MRSEC DMR-0819860, Packard Foundation, and a Keck grant. XD is supported by the National Natural Science Foundation of China, the 973 program of China (No. 2011CBA00108 and No. 2013CB921700), and the "Strategic Priority Research Program (B)" of the Chinese Academy of Sciences (No. XDB07020100).

-
- [1] G. Volovik, *The Universe in a Helium Droplet* (Oxford University Press New York, 2009).
 - [2] Z. Wang, Y. Sun, X.-Q. Chen, C. Franchini, G. Xu, H. Weng, X. Dai, and Z. Fang, *Physical Review B* **85**, 195320 (2012).
 - [3] Z. Liu, B. Zhou, Y. Zhang, Z. Wang, H. Weng, D. Prabhakaran, S.-K. Mo, Z. Shen, Z. Fang, X. Dai, *et al.*, *Science* **343**, 864 (2014).
 - [4] Z. Wang, H. Weng, Q. Wu, X. Dai, and Z. Fang, *Physical Review B* **88**, 125427 (2013).
 - [5] S. Borisenko, Q. Gibson, D. Evtushinsky, V. Zabolotnyy, B. Büchner, and R. J. Cava, *Phys. Rev. Lett.* **113**, 027603 (2014).
 - [6] T. Liang, Q. Gibson, M. N. Ali, M. Liu, R. Cava, and N. Ong, *Nature materials* **14**, 280 (2015).
 - [7] M. Neupane, S.-Y. Xu, R. Sankar, N. Alidoust, G. Bian, C. Liu, I. Belopolski, T.-R. Chang, H.-T. Jeng, H. Lin, *et al.*, *Nature communications* **5** (2014).
 - [8] Z. Liu, J. Jiang, B. Zhou, Z. Wang, Y. Zhang, H. Weng, D. Prabhakaran, S. Mo, H. Peng, P. Dudin, *et al.*, *Nature materials* **13**, 677 (2014).
 - [9] X. Wan, A. M. Turner, A. Vishwanath, and S. Y. Savrasov, *Physical Review B* **83**, 205101 (2011).
 - [10] G. Xu, H. Weng, Z. Wang, X. Dai, and Z. Fang, *Physical review letters* **107**, 186806 (2011).
 - [11] A. Burkov and L. Balents, *Physical review letters* **107**, 127205 (2011).
 - [12] K.-Y. Yang, Y.-M. Lu, and Y. Ran, *Physical Review B* **84**, 075129 (2011).
 - [13] J. Liu and D. Vanderbilt, *Physical Review B* **90**, 155316 (2014).
 - [14] M. Hirayama, R. Okugawa, S. Ishibashi, S. Murakami, and T. Miyake, *Physical Review Letters* **114**, 206401 (2015).
 - [15] S.-M. Huang, S.-Y. Xu, I. Belopolski, C.-C. Lee, G. Chang, B. Wang, N. Alidoust, M. Neupane, H. Zheng, D. Sanchez, *et al.*, arXiv preprint arXiv:1503.05868 (2015).
 - [16] H. Weng, C. Fang, Z. Fang, B. A. Bernevig, and X. Dai, *Phys. Rev. X* **5**, 011029 (2015).
 - [17] S.-M. Huang, S.-Y. Xu, I. Belopolski, C.-C. Lee, G. Chang, B. Wang, N. Alidoust, G. Bian, M. Neupane, A. Bansil, *et al.*, *Nature Comm.* **6**, 7373 (2015).
 - [18] S.-Y. Xu, I. Belopolski, N. Alidoust, M. Neupane, C. Zhang, R. Sankar, S.-M. Huang, C.-C. Lee, G. Chang, B. Wang, *et al.*, arXiv preprint arXiv:1502.03807 (2015).
 - [19] B. Lv, H. Weng, B. Fu, X. Wang, H. Miao, J. Ma, P. Richard, X. Huang, L. Zhao, G. Chen, *et al.*, arXiv preprint arXiv:1502.04684 (2015).
 - [20] S.-M. Huang, S.-Y. Xu, I. Belopolski, C.-C. Lee, G. Chang, B. Wang, N. Alidoust, M. Neupane, H. Zheng, D. Sanchez, *et al.*, arXiv preprint arXiv:1503.05868 (2015).
 - [21] T. T. Heikkilä, N. B. Kopnin, and G. E. Volovik, *JETP letters* **94**, 233 (2011).
 - [22] M. Silaev and G. Volovik, *Physical Review B* **86**, 214511 (2012).
 - [23] A. A. Abrikosov, *Phys. Rev. B* **58**, 2788 (1998).
 - [24] H. B. Nielsen and M. Ninomiya, *Physics Letters B* **130**, 389 (1983).
 - [25] A. Zyuzin and A. Burkov, *Physical Review B* **86**, 115133 (2012).
 - [26] P. Hosur and X. Qi, *Comptes Rendus Physique* **14**, 857 (2013).
 - [27] G. Volovik, *JETP Letters* **98**, 753 (2014).
 - [28] C. Zhang, S.-Y. Xu, I. Belopolski, Z. Yuan, Z. Lin, B. Tong, N. Alidoust, C.-C. Lee, S.-M. Huang, H. Lin, *et al.*, arXiv preprint arXiv:1503.02630 (2015).
 - [29] J. Xiong, S. K. Kushwaha, T. Liang, J. W. Krizan, W. Wang, R. Cava, and N. Ong, arXiv preprint arXiv:1503.08179 (2015).
 - [30] X. Huang, L. Zhao, Y. Long, P. Wang, D. Chen, Z. Yang, H. Liang, M. Xue, H. Weng, Z. Fang, *et al.*, arXiv preprint arXiv:1503.01304 (2015).
 - [31] G. B. Halász and L. Balents, *Physical Review B* **85**, 035103 (2012).
 - [32] M. N. Ali, J. Xiong, S. Flynn, J. Tao, Q. D. Gibson, L. M. Schoop, T. Liang, N. Haldolaarachchige, M. Hirschberger, N. Ong, *et al.*, *Nature* **514**, 205 (2014).
 - [33] Z. J. Wang, A. A. Soluyanov, M. Troyer, X. Dai, and B. A. Bernevig, in preparation.
 - [34] A. A. Soluyanov, M. Troyer, X. Dai, and B. A. Bernevig, in preparation.
 - [35] C. L. Kane and E. J. Mele, *Phys. Rev. Lett.* **95**, 146802 (2005).
 - [36] A. A. Soluyanov and D. Vanderbilt, *Phys. Rev. B* **83**, 235401 (2011).
 - [37] R. Yu, X. L. Qi, A. Bernevig, Z. Fang, and X. Dai, *Phys. Rev. B* **84**, 075119 (2011).
 - [38] L. Fu and C. L. Kane, *Phys. Rev. B* **74**, 195312 (2006).
 - [39] D. Gresch, A. A. Soluyanov, G. Autés, D. Vanderbilt, B. A. Bernevig, O. Yazyev, and M. Troyer, "Universal Framework for Computing Topological Invariants of Band Structures and its Numerical Implementation – Z2Pack," in preparation.
 - [40] B. E. Brown, *Acta Crystallographica* **20**, 268 (1966).
 - [41] W. Dawson and D. Bullett, *Journal of Physics C: Solid State Physics* **20**, 6159 (1987).

- [42] A. Mar, S. Jobic, and J. A. Ibers, Journal of the American Chemical Society **114**, 8963 (1992).
- [43] G. Kresse and J. Furthmüller, Computational Materials Science **6**, 15 (1996).
- [44] P. E. Blöchl, Physical Review B **50**, 17953 (1994).
- [45] G. Kresse and D. Joubert, Physical Review B **59**, 1758 (1999).
- [46] J. P. Perdew, K. Burke, and M. Ernzerhof, Physical review letters **77**, 3865 (1996).
- [47] I. Souza, N. Marzari, and D. Vanderbilt, Phys. Rev. B **65**, 035109 (2001).
- [48] A. A. Mostofi, J. R. Yates, G. Pizzi, Y.-S. Lee, I. Souza, D. Vanderbilt, and N. Marzari, *Computer Physics Communications* **185**, 2309 (2014).
- [49] A. A. Soluyanov and D. Vanderbilt, Phys. Rev. B **83**, 035108 (2011).
- [50] R. D. King-Smith and D. Vanderbilt, Phys. Rev. B **47**, 1651 (1993).
- [51] P. Ramachandran and G. Varoquaux, Computing in Science & Engineering **13**, 40 (2011).
- [52] K. Momma and F. Izumi, Journal of Applied Crystallography **44**, 1272 (2011)

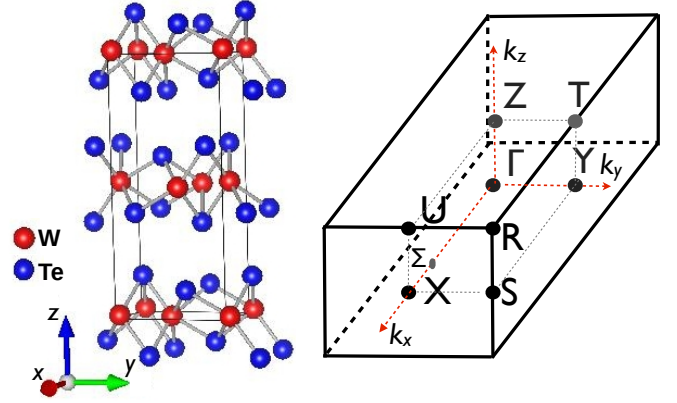


Figure 6. Left panel: crystal structure of WTe_2 . Right panel: Brillouin zone of the rhombohedral unit cell.

Appendix A: Crystal structure and computation details

The crystal structure of WTe_2 and its Brillouin zone are illustrated in Fig. 6. For completeness, we list the experimental structural parameters taken from Ref. [42] that were used in this work. The lattice constants are $a = 3.477$, $b = 6.249$ and $c = 14.018$, and both W and Te atoms occupy $2a$ Wyckoff positions corresponding to $(0, y, z)$ and $(1/2, -y, z + 1/2)$. Values of x and y for this structure are listed in Table I.

	W(1)	W(2)	Te(1)	Te(2)	Te(3)	Te(4)
y	0.60062	0.03980	0.85761	0.64631	0.29845	0.20722
z	0.5	0.01522	0.65525	0.11112	0.85983	0.40387

Table I. Positions of atoms in the unit cell of WTe_2 given as coordinates for Wyckoff positions $2a$ of the $Pnm2_1$ space group. Bracketed numbers following the element symbol indicate distinct Wyckoff positions. There are two distinct Wyckoff positions for W and four for Te atoms.

Band structure calculations (both with and without spin-orbit coupling (SOC)) were performed in VASP [43] *ab initio* code using PAW [44, 45] pseudopotentials with $6s^25d^4$ and $5s^25p^4$ valence electron configurations for W and Te correspondingly. The PBE [46] approximation was used. Spin-orbit coupling was implemented in pseudopotentials. The energy cutoff was taken to be 260eV. Gaussian smearing of width 0.05eV and a $12 \times 10 \times 6$ Γ -centered k -point mesh were used to perform Brillouin zone integrations. The conclusions of the paper were also verified using a more elaborate pseudopotential for W with semicore p -states included in the valence, that is with $5p^66s^25d^4$ valence electron configuration.

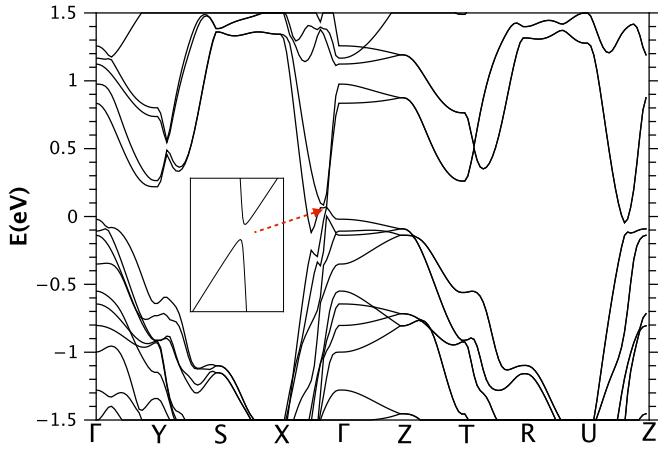


Figure 7. Band structure of WTe₂ without SOC. E_F is set to 0.

Appendix B: Electronic structure without spin-orbit coupling

The band structure of WTe₂ in the absence of SOC is shown in Fig. 7. To understand the nature of crossings in this case we carried out an extensive symmetry analysis that will be reported elsewhere [33]. Here we only state the main conclusions. Using a two band model

$$H(k_x, k_y, k_z) = \varepsilon(k_x, k_y, k_z) + \sum_{i=x,y,z} d_i(k_x, k_y, k_z) \sigma_i, \quad (\text{B1})$$

where σ_i are the Pauli matrices, one can show that on the $k_z = 0$ plane only two of the three d_i coefficients are linearly independent. The degeneracy occurs if for some (k_x, k_y) both of these coefficients vanish. Thus, there are two independent constraints on two functions of k_x, k_y , the codimension is zero, and the solution is in general possible at isolated points in the $k_z = 0$ plane. In addition, it can be shown that without SOC no band crossings can generally occur along the $\Gamma - X$ axis. Indeed, *ab initio* results show that a small band gap exists in the band structure along $\Gamma - X$, as illustrated in the inset of Fig. 7.

First-principles calculations support our conclusions. Without SOC we find 8 Weyl points (not accounting for spin) in the $k_z = 0$ plane. In addition, we find 8 more spinless Weyls at low symmetry points $k_i \neq 0$ for all i . The coordinates of Weyl points and their Chern numbers are given in Tab. II.

Now, when spin is taken into consideration but SOC is still neglected, each Weyl point becomes doubled, with doubled chirality due to SU(2) symmetry. When SOC is gradually increased the Weyl points split and start moving in the Brillouin zone. For a material with weak SOC, one can expect this motion to be the only effect of SOC, so that the Weyl points do not vanish in general. In WTe₂, however, SOC is large. To see its effect on the structure of Weyl points in the BZ, we carried out a

	k_x	k_y	k_z	C
1	0.1054	0.0087	0	+1
2	0.1742	0.1200	0	+1
3	0.14992	0.07845	0.2329936	-1
4	0.14992	0.07845	-0.2329936	-1

Table II. Coordinates and Chern numbers of 4 out of 16 Weyl points appearing without SOC. The other 12 points are related by the ones listed by reflections being located at $(-k_x, k_y, k_z)$, $(k_x, -k_y, k_z)$ with Chern numbers $-C$ and at $(-k_x, -k_y, k_z)$ with Chern number C . Points at $k_z \neq 0$ are symmetric about the xy -plane due to the compound symmetry formed by time reversal and two-fold rotation.

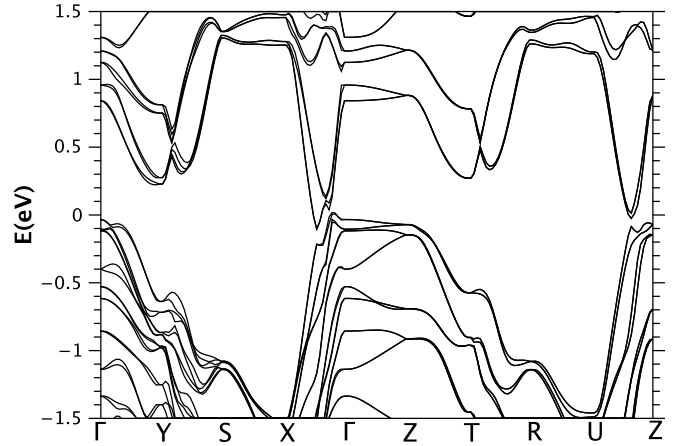


Figure 8. Band structure of WTe₂ with SOC taken into account. E_F is set to 0.

smooth interpolation between no SOC and full SOC band structures. In the process, other Weyl points appear and disappear (by merging points with opposite chiralities), so that the final arrangement of Weyl points reported in the main text cannot be understood in terms of rearranging the Weyl points that are present in the absence of SOC.

Appendix C: Electronic structure with spin-orbit coupling

The fully relativistic band structure is illustrated in Fig. 8. Symmetry considerations indicate the possibility to have locally stable point-like degeneracies in the $k_z = 0$ plane, where a little group formed by a combination of a two-fold rotation and time-reversal exists [33]. As will be explained elsewhere in detail, this suggests that double degeneracies can occur at isolated points in the $k_z = 0$ plane.

In accord with this argument, eight Weyl points (listed in Tab. III), described in the main text, are indeed located in the $k_z = 0$ plane. A general form of the Hamil-

	k_x	k_y	k_z	C
1	0.12184	0.03825	0	+1
2	0.12141	0.0454	0	-1

Table III. Coordinates and Chern numbers of 2 out of 8 Weyl points appearing with SOC. The other 6 points are related by the ones listed by reflections, being located at $(-k_x, k_y, k_z)$, $(k_x, -k_y, k_z)$ with Chern numbers $-C$.

tonian around a Weyl point in the $k_z = 0$ plane can be constructed using the following two dimensional representation for the combination of C_2 and time-reversal

$$C_{2T} = -i\sigma_z K \quad (C1)$$

where K is complex conjugation. This form of the symmetry can be shown to be consistent with the representations of other symmetries in this non-symmorphic space group.

Keeping only terms linear in k and subjecting the Hamiltonian to this symmetry we find the general form of the Hamiltonian around a Weyl point in $k_z = 0$ with SOC

$$H(\mathbf{k}) = \epsilon(\mathbf{k}) + (ak_x + ck_y)\sigma_y + (bk_x + dk_y)\sigma_z + ek_z\sigma_x \quad (C2)$$

where

$$\epsilon(\mathbf{k}) = Ak_x + Bk_y \quad (C3)$$

For the Weyl point to be of type II, the kinetic part of the energy should dominate over the potential one in at least some direction in k -space. To find such directions for the points in question, we plotted the ratio

$$R = \frac{(Ak_x + Bk_y)^2}{e^2 k_z^2 + (ak_x + ck_y)^2 + (bk_x + dk_y)^2} \quad (C4)$$

on the circles defined by $k_x^2 + k_y^2 = 10^{-6}$, where k_x and k_y are taken in reduced coordinates, and the constants are explained in the main text. The results are illustrated in Fig. 9. The region, where $R > 1$, meaning that the kinetic energy dominates and the Weyl points are of type II, is shown in red.

Finally, we fitted the Hamiltonian of Eq. C2 to the first-principles band structure around the Weyl points to get the values of its parameters. They are provided in Tab. IV.

Appendix D: Computation of chiralities of type-II Weyl points

The Fermi surface of a type-II Weyl point is open, so it cannot be used for integrating the Berry curvature in chirality computation. Instead, the Berry curvature of N bands, where N is the number of electrons per unit cell, should be integrated over a surface, on which these

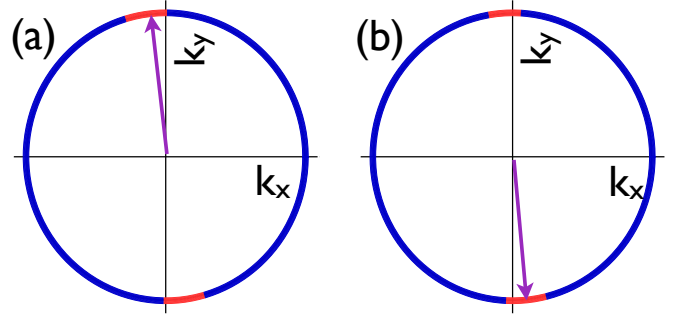


Figure 9. The ratio R of Eq. C4 for the circle of radius 10^{-3} drawn around the two Weyl points. Red color corresponds to $R > 1$, while blue is $R < 1$. The arrows show the direction from one of the two points to the other. Panel (a): Weyl point at $(0.12184, 0.03825, 0)$. Panel (b): Weyl point at $(0.12141, 0.0454, 0)$.

point	A	B	a	b	c	d	e
1	-2.739	0.612	0.987	1.107	0.0	0.270	0.184
2	1.204	0.686	-1.159	1.046	0.0	0.055	0.237

Table IV. Parameter values for the Hamiltonian of Eq. C2 around the two Weyl points given in [eVÅ]. Point 1 refers to the Weyl at $(0.12184, 0.03825, 0)$, while point 2 is $(0.1241, 0.0454, 0)$.

N bands are separated by an energy gap from the higher energy ones. Since the crossing of the N th and $N + 1$ th bands occurs at a point (Weyl point), such a surface enclosing the type-II Weyl point always exists. The calculation becomes equivalent to the usual integration over the occupied bands, if one allows for a k -dependent chemical potential, located in between the N -th and $N + 1$ -th bands at each k -point on the surface.

Following this prescription and using a Wannier function-based tight-binding model [47, 48] described below, Bloch states were calculated on the spheres around the gapless points. The Hamiltonian remained gapped in the above sense ($N = 72$) everywhere on these spheres, schematically illustrated as $\ell_{1,2}$ in Fig. 3(a) of the main text. The corresponding flux of Berry curvature was computed by discretizing a closed sphere, parametrized by angles θ and ϕ , into 1D-loops, as shown in Fig. 10(a). When traversed around a loop, the occupied Bloch states accumulate a Berry phase, the trace of which is computed for each of these loops θ_i using the methods of Refs. [36, 37, 49].

These Berry phases correspond to the average position of charge [50], associated with the bands below the gap, on the loop, $\langle \varphi \rangle(\theta_i)$. Since 1D loops cover a closed surface, the center of charge $\langle \varphi \rangle$ can only shift by an integer multiple of 2π when θ varies from 0 to π . This multiple is equal to the monopole charge enclosed and gives the chirality of the WP enclosed. Similar considerations are

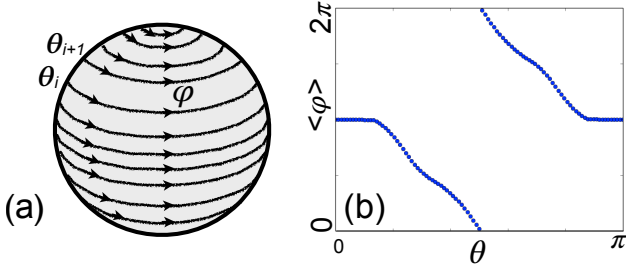


Figure 10. Panel (a): schematic illustration of the integration paths used to calculate topological charges of Weyl points. Panel (b): motion of the center of charge around the sphere is shown schematically for ℓ_1 in panel (a) of Fig. 3 of the main text. The Chern number of the enclosed Weyl point is equal to -1 .

used when computing Chern numbers of insulators, with the only difference that the BZ in that case is a torus, rather than a sphere. The result of such a calculation is equivalent to taking the surface integral of the Berry curvature over a closed surface. A more detailed account of this type of calculations, along with the rigorous derivation can be found in Ref. [?].

The results obtained for WTe_2 is shown in Fig. 10(b) for the sphere ℓ_1 of Fig. 3(a) of the main text. The charge center shifts downwards, corresponding to Chern number $C = -1$, thus proving the existence of a WP of negative chirality inside ℓ_1 . For the sphere ℓ_2 , enclosing the second Weyl point, the Chern number is $C = +1$, and hence the chirality of this point is positive.

Appendix E: Tight-binding models

To compute chiralities of Weyl points, as well as to interpolate between no SOC and full SOC states, tight-binding models were derived with and without SOC. These tight-binding models were obtained using Wannier interpolation [47, 48]. Bloch states were projected onto all W d -states and all Te p -states. We used a specially symmetrized model without SOC that has the same Weyl points distribution as obtained from first-principles, and interpolated it to the one derived from a fully relativistic calculation.

To get the chiralities of Weyl points for the full SOC case, we used an 88-band tight binding model derived

from the full SOC first-principles calculation.

Appendix F: Surface states

Here we provide an illustration to support our assertion, made in the main text, about the possibility to move the Fermi arc that crosses the hole pocket into the continuum of the bulk states. Fig. 11 shows a larger scale

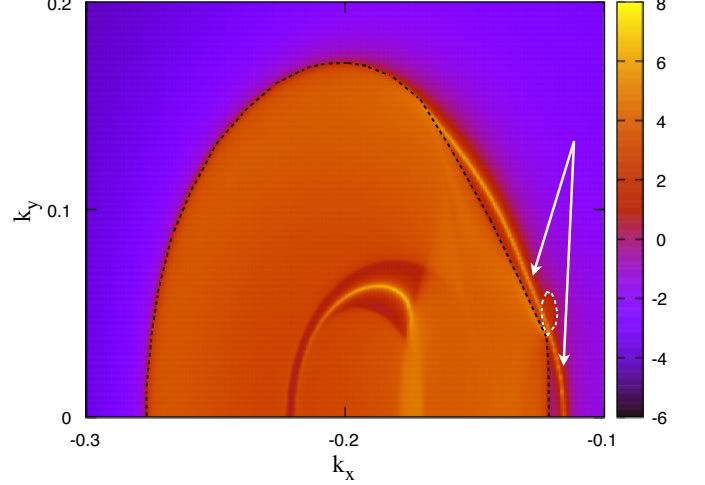


Figure 11. Spectral function illustrates the surface Fermi surface. The surface state, indicated with arrows, emerges in the electron pocket (shown with the black contour), crosses the hole pocket (shown with the white contour), and merges back into the electron pocket (by mirror symmetry).

illustration, where it can be seen that this surface state emerges from the electron pocket and merges back into it. Note that unlike the illustration of Fig. 4(b) of the main text, the small electron pocket becomes part of the larger electron pocket in this illustration. This is due to small deviations ($\approx 10\text{meV}$) of our tight-binding model band structure from its *ab initio* counterpart used for illustrations in Fig. 4 of the main text.

Appendix G: Additional Remarks

Mayavi [51] and VESTA [52] software packages were used to create some of the illustrations.